Site selection for desert wind and solar farms based on heterogeneous sand flux

Guoshuai Li[1, 2], Lihai Tan[3], Bao Yang[4], Tao Che[1], Guangcai Feng[5], Fredrik Charpentier Ljungqvist[6, 7, 8], Yayong Luo[9], Heqiang Du[10], Hui Zhao[10], Ying Zhang[1], Chunlin Huang[1], Ning Huang[11], Wenjun Tang[2], Rui Jin[1], and Xin Li[2]

[1]Heihe Remote Sensing Experimental Research Station, Northwest Institute of Eco-Environment and Resources, Chinese Academy of Sciences, Lanzhou, China
[2]National Tibetan Plateau Data Center, State Key Laboratory of Tibetan Plateau Earth System, Environment and Resources, Institute of Tibetan Plateau Research, Chinese Academy of Sciences, Beijing, China
[3]Dunhuang Gobi Desert Research Station, Northwest Institute of Eco-Environment and Resources, Chinese Academy of Sciences, Lanzhou, China
[4]School of Geography and Ocean Science, Nanjing University, Nanjing, China
[5]School of Geosciences and Info-physics, Central South University, Changsha, China
[6]Department of History, Stockholm University, Stockholm, Sweden
[7]Bolin Centre for Climate Research, Stockholm University, Stockholm, Sweden
[8]Swedish Collegium for Advanced Study, Uppsala, Sweden
[9]Naiman Desertification Research Station, Northwest Institute of Eco-Environment and Resources, Chinese Academy of Sciences, Lanzhou, China
[10]Key Laboratory of Desert and Desertification, Northwest Institute of Eco-Environment and Resources, Chinese Academy of Sciences, Lanzhou, China
[11]Department of Mechanics, College of Civil Engineering and Mechanics, Lanzhou University, Lanzhou, China

Correspondence to: Xin Li, xinli@itpcas.ac.cn

Abstract

Site selection is a priority for building wind and solar farms in deserts, which has to consider the dune threats associated with sand flux, such as dust contamination and sand burial. Thus, understanding changes in sand flux can optimize the site selection for wind and solar farms in deserts. Here, we use the ERA5-Land hourly wind data with 0.1°×0.1° resolution to calculate the yearly sand flux for the period 1950–2021, and adopt the mean of sand flux to score the suitability of global deserts for wind and solar farms. We find that global deserts are dominated by low flux potential (≤20 m^2 yr^{-1}) and resultant flux potential (≤1.0 m^2 yr^{-1}) over the past 72 years, and the scoring result indicates that most deserts have low suitability for building wind farms, and high suitability for building solar farms. Our study optimizes the site selection for wind and solar farms in deserts, and contributes to achieving the affordable and clean energy target by 2030 under the framework of the United Nations sustainability development goals.

INTRODUCTION

Increasing the share of renewable energy is essential to realize the global emission reduction targets[1, 2]. According to the current global emission reduction trends, it is difficult to achieve the global 1.5°C/2°C temperature increase goals and 2050/2070 net-zero emission targets[3-5]. To reduce anthropogenic carbon dioxide emissions, the exploration of renewable energy at a global scale need be strengthened[1, 6, 7]. In recent years, wind and solar energy, as affordable and clean energy, has been increasingly utilized[8]. A large number of wind and solar farms have been built across the globe[9]. Deserts with low land value, intermittently high wind speed and long sunshine time are favorable locations for building wind and solar farms[10, 11]. In turn, wind and solar farms can increase surface friction, reduce surface albedo, enhance local precipitation in deserts, and flourish regional vegetation around deserts[10]. Hence, desert wind and solar geoengineering should be considered one of the feasible action programs of planetary geoengineering[12, 13] aiming at mitigating anthropogenic greenhouse gas emissions. For building wind and solar farms in deserts, the existing site suitability methodologies[14-16] do not effectively solve the dune threats (e.g. dust contamination and sand burial) to wind and solar generation infrastructure across global deserts.

Dune threats are associated with sand flux, and sand flux driven by effective friction velocities reflects the potential sediment transport capacity of the wind[17-24]. Similar to the drift potential and resultant drift potential of sand drift[25, 26], the absolute potential sand flux and resultant potential sand flux[18-20], sand flux in this study can be briefly quantified through the flux potential (FP) and resultant flux potential (RFP). The FP is the sum of volume fluxes in all azimuths, and RFP is calculated by the Euclidean formula of the projected due-north and due-east volume flux components from all azimuths (METHODS). Note that the flux calculation here is for the saturated flux, and the true flux may be smaller (due to precipitation or erodible surface fraction) or larger (due to dune steepness), but this is a reasonable estimate with precedents in other studies[18-21]. The FP and RFP of sand flux have been used to quantify dune activities[18-21]. Theoretically, the FP represents wind energy, so higher FP brings severer sandblasting[27, 28], produces more dusts and causes severer sand burial[25, 26]; RFP represents the net sand transport potential in the resultant flux direction, so higher RFP means larger possibilities of sand burial; FP is more important than RFP in assessing the dune threats. Most studies of sand flux are based on the wind data from local meteorological stations[29]. The number of global meteorological stations is limited in desert environments. Wind data from the reanalysis products with different spatiotemporal resolutions provide a feasible scheme for quantifying sand flux at a global scale[18-21]. For example, the ERA5 reanalysis product (0.25°×0.25° resolution)[30] was used to calculate the FP and RFP of sand flux[18-20]. Accordingly, the hourly wind data from the ERA5-Land reanalysis product with higher resolution (0.1°×0.1°)[31] should be able to adequately capture more spatiotemporal details of changes in sand flux[21], and then assess the dune threats to wind and solar farms in deserts. However, how to use the FP and RFP to effectively optimize the site selection for wind and solar farms across global deserts remains unsolved.

In this study, we use the eastward and northward wind components at the height of 10 m from the ERA5-Land hourly wind data to calculate the yearly sand flux for the period 1950–2021, and adopt the 72-yr mean of sand flux to assess the suitability of global deserts for building wind and solar farms. According to wind and solar farm scores, we can reduce or avoid the dune threats, and efficiently implement wind and solar farms in deserts.

Results

72-yr mean of sand flux

The resampled global deserts with 0.1°×0.1° resolution were distributed in 55 countries, including 24 countries in Asia, 21 countries in Africa, 5 countries in South America, 2 countries in North America, 2 countries in Europe and 1 country in Australasia (Fig. 1).

After calculating the yearly FP on the basis of the ERA5-Land hourly wind data (METHODS), we find that during 1950–2021, the FP mean of global deserts was 9.5±2.0 m^2 yr^{-1} (mean ± standard deviation). Across global deserts, the FP mean and standard deviation were as high as 180.0 m^2 yr^{-1} and 16.9 m^2 yr^{-1}, respectively. The FP means of global deserts had patch distributions. In terms of the ERA5-Land grid cell number, the FP means of 0–10 m^2 yr^{-1} were dominant, and followed by the patches of 10–20 m^2 yr^{-1}. The FP means greater than 20 m^2 yr^{-1} were mainly observed in northern Somalia, middle and northwest Chad, southern Tunisia, middle Algeria, northern and western Western Sahara, middle and northwest Mauritania, southwest Morocco of Africa; in northern and western China, southern Mongolia, southern and southwest Kazakhstan, western Afghanistan, eastern Iran and southeast Oman of Asia; in middle United States of North America; in southern Argentina of South America and in southern and western Australia (Fig. 2a).

The RFP mean of global deserts was 0.4±0.2 m^2 yr^{-1}, and the maximum mean and standard deviation of RFP were 7.6 m^2 yr^{-1} and 3.1 m^2 yr^{-1}, respectively. The RFP means of global deserts also had obvious patch distributions. The RFP means of most deserts were dominated by the patches of 0–0.5 m^2 yr^{-1}, and then the patches of 0.5–1.0 m^2 yr^{-1}. The patches with the RFP mean greater than 1.0 m^2 yr^{-1} were most observed in northern Somalia, middle and northwest Chad, northern and western Western Sahara, northwest Mauritania and southwest Morocco of Africa; in northern and western China, southern Mongolia, western Afghanistan, eastern Iran and southeast Oman of Asia (Fig. 2b). The patches with high RFP mean may have high dune celerities[32]. For the spatial distributions of the FP and RFP standard deviations, see Fig. S1.

Scoring scheme for desert wind and solar farms

We classified the 72-yr mean of sand flux to construct a scoring scheme. First, the FP means were used to distinguish the dust contamination and sand burial, and the RFP means were used to quantify the sand burial. Then, we intersected the above two mean classifications, removed the non-observed intersections and scored the suitability according to the established rules, in which we assumed that FP mean is more important than RFP mean in scoring the suitability of wind and solar farms (METHODS).

More specifically, the first step of our scoring scheme is to divide the FP means into 18 classifications with the spacing of 10 m^2 yr^{-1}. The grid cell numbers of these classifications and the corresponding percentages accounting for the global desert grid cell number (174884) from low to high were 113077, 64.66%; 47283, 27.04%, 9480, 5.42%; 2493, 1.43%; 858, 0.49%; 548, 0.31%; 433, 0.25%; 262, 0.15%; 229, 0.13%; 97, 0.06%; 41, 0.02%; 33, 0.02%; 15, 0.01%; 11, 0.1%; 6, 0.00%; 8, 0.00%; 4, 0.00% and 6, 0.00%, respectively (Fig. 3a). The second step is to divide the RFP means into 8 classifications with the spacing of 1.0 m^2 yr^{-1}. Similarly, the numbers and percentages of these classifications from low to high were 170939, 97.74%; 3268, 1.87%; 408, 0.23%; 144, 0.08%; 82, 0.05%; 29, 0.02%; 9, 0.01% and 5, 0.00%; respectively (Fig. 3b). These statistics showed that global deserts are dominated by low FP (≤20 m^2 yr^{-1}) and RFP (≤1.0 m^2 yr^{-1}). The final step is to intersect the classifications of FP and RFP means. We removed the non-observed intersections and got the scores of wind and solar farms according to the established rules (Table S1 and Table S3, more details see METHODS). The ascending FP mean classifications are favorable for wind farms, but not for solar farms. The ascending RFP mean classifications are more unfavorable for solar farms than wind farms.

We find that wind and solar farm scores across global deserts had the differentiated spatial distributions due to different FP and RFP mean classifications. The maximum scoring frequencies for wind farms (Fig. 3c inset) and solar farms (Fig. 3d inset)

(64.66%) were the same, but their scores were 2 and 80, respectively. The frequencies of score 1–4 (64.72%), 5–8 (27.26%), 9–12 (5.2%) for wind farms were greater than 5% (Fig. 3c), and those of score 77–80 (91.69%), 73–76 (5.42%) for solar farms were greater than 5% (Fig. 3d). If only consider the dune threats, wind farms had more low scores (i.e. low suitability), and solar farms had more high scores (i.e. high suitability); and the scoring frequency distributions of global deserts presented the similar situation (Fig. 3c inset and Fig. 3d inset). However, in the deserts with high FP mean, such as in northern Somalia, middle Chad and western Western Sahara, western Afghanistan and northern China, wind farms (Fig. 3c) had higher scores than solar farms (Fig. 3d). In conclusion, the criteria of site selection for wind and solar farms varied across the globe.

DISCUSSION

Our results first demonstrate heterogeneous spatial distributions of sand flux and classifications of global deserts in terms of wind environments, and present a scoring scheme for the site selection of wind and solar farms across global deserts on the basis of the 72-yr mean of sand flux, which can reflect the basic characteristics of sand flux. In this study, we assumed that FP mean is more important than RFP mean in evaluating the threats to wind and solar generation infrastructure. Higher FP brings severer sandblasting[27, 28], produces more dust and causes severer sand burial to low solar photovoltaic panel; higher RFP causes severer sand burial to low solar photovoltaic panel than high and large wind turbine[8] in the resultant flux direction. In addition, we adopt the equidistant spacings of 10 m^2 yr^{-1} and 1 m^2 yr^{-1} in FP and RFP mean classifications to ensure the rationality of scoring scheme. Furthermore, we find that 82% of the existing solar farm sites[33] in deserts are located in the highest-score regions of solar farms (Fig. S2).

This study provides a guide to select the regions in deserts suitable for wind farms or solar farms. The expanding use of wind data from the reanalysis products with different spatiotemporal resolutions[18-21], especially, the ERA5-Land reanalysis product (0.1°×0.1° and hourly resolution)[21], could better characterize the wind environments and quantify the dune threats at a global scale. Some deserts have no effective friction velocities and small or zero flux[18-20, 26]. They may be interpreted as the ancient dune systems or be driven by other episodic factors (e.g. alluvial/fluvial, lacustrine and coastal). But this study only focuses on the potential sediment transport capacity determined by effective friction velocities[17-24]. In the actual site selection, local situations such as sediment availability[32], topographic influences[35, 36] and precipitation effect[19, 37] should also be considered.

Our scoring scheme could be used to choose the best sites for wind and solar farms in the regions affected by dune threats, and to help assess the site suitability of traffic engineering, petroleum exploitation and irrigated farming in desert environments. Expectantly, our results can help build desert wind and solar geoengineering and achieve the Sustainable Development Goal 7 ("affordable, reliable, sustainable and modern energy for all") by 2030[38], and even contributes to achieve the global surface temperature goal of 1.5–2°C and reach the global carbon neutrality[39] in a long-term perspective.

METHODS

Desert data

Deserts are from the global and regional desert area, which was extracted by support vector machine analysis, trial-and-error method and visual interpretation analyses based on the Moderate Resolution Imaging Spectroradiometer data (500 m resolution)[40]. We resampled the data into grid cells at 0.1°×0.1° resolution, same to the spatial resolution of the ERA5-Land reanalysis product from the European Center for Medium Range Weather Forecasts[31]. Furthermore, we used the 72-yr FP mean to constrain global deserts. The total number of grid cells for global dunes was 174884.

Wind data

Wind data are from the eastward and northward wind components at the height of 10 m of the ERA5-Land reanalysis product, which has the hourly temporal resolution and 0.1°×0.1° spatial resolution[31]. In this study, the ERA5-Land hourly wind data spanned from 1950 to 2021. The instantaneous wind speed U and azimuth A at the height of 10 m is calculated as

$$U = \sqrt[2]{u^2 + v^2} \quad (1)$$

$$A = atan2(u, v) \quad (2)$$

where u is the eastward component, in m s^{-1}; and v is the northward component, in m s^{-1}.

Conceptual framework of sand flux

The friction velocity u_{fv} in m s^{-1} is calculated as

$$u_{fv} = \frac{U\kappa}{ln(z/z_0)} \quad (3)$$

where U is the instantaneous wind speed at the height of 10 m, κ = 0.4 is Von Kármán constant, z = 10 m is the height above the Earth surface, z_0 = 0.001 m is the assumed roughness length above the sand surface[41].

The threshold friction velocity u_{tfv} = 0.277 m s^{-1} is calculated by

$$u_{tfv} = \frac{\sqrt[2]{gd\rho_s/\rho_f}}{10} \tag{4}$$

where g = 9.81 m^2 s^{-1} is gravity acceleration; d = 0.00036 m is the mean of median grain diameters for surface samples in the study of Martin and Kok (0.53±0.04 mm, 0.53±0.03 mm and 0.40±0.07 mm)[23], Greeley et al. (0.23 mm)[42], Namikas (0.25 mm)[43] and Chinese deserts (the mean of median grain diameters of 426 dune samples is 0.23±0.06 mm) in this study (Table S4); ρ_s = 2650 kg m^{-3} is sand density; ρ_f = 1.22 kg m^{-3} is air density[23].

The saturated mass flux $\overrightarrow{q_m}$ in kg m^{-1} s^{-1} is approximately[22-24]

$$\overrightarrow{q_m} = C\frac{u_{tfv}}{g}\rho_f\left(u_{efv}^2 - u_{tfv}^2\right) \tag{5}$$

where C = 5 is an empirical (dimensionless) scaling parameter, $u_{efv} > u_{tfv}$ is effective friction velocity. Divided by sand density ρ_s, the mass flux measured in kg m^{-1} s^{-1} is converted to volume flux measured in m^2 s^{-1}, so the volume flux $\overrightarrow{q_v}$ is defined as

$$\overrightarrow{q_v} = C\frac{u_{tfv}}{g\rho_s}\rho_f\left(u_{efv}^2 - u_{tfv}^2\right) \tag{6}$$

After deriving instantaneous effective friction velocity, and considering the intermittence of winds, we also define $\overrightarrow{q_v} = 0$ when $u_{fv} \leq u_{tfv}$, and finally apply zero flux to the mean of the subsequent flux calculations, so the flux potential (FP) measured in m^2 yr^{-1} is given by

$$\mathrm{FP} = S\frac{\sum_{i=1}^{N}|\overrightarrow{q_v}|}{N} \tag{7}$$

where FP reflects the potential sediment transport capacity of effective friction velocities, S = 31536000 is the number of seconds of 365 days, N is the number of hours of Julian years (8760 hours for common year or 8784 hours for leap year) for the period 1950–2021.

The obtained $\overrightarrow{q_b}$ in all azimuths (A) from the 10 m instantaneous effective friction velocities are projected to the due-east and due-north directions to solve the resultant flux potential (RFP) measured in m^2 yr^{-1},

$$\mathrm{RFP\_E} = S\frac{\sum_{i=1}^{N}\overrightarrow{q_v}\sin A}{N} \tag{8}$$

$$\mathrm{RFP\_N} = S\frac{\sum_{i=1}^{N}\overrightarrow{q_v}\cos A}{N} \tag{9}$$

$$\mathrm{RFP} = \sqrt[2]{\mathrm{RFP\_E}^2 + \mathrm{RFP\_N}^2} \tag{10}$$

where RFP is the Euclidean sum of the projected due-east and due-north volume flux components (RFP_E and RFP_N). It represents the net sand transport potential in the resultant flux direction, which is the net trend of sand flux, in line with the dominant direction of dune celerities. We used the absolute RFP, neglecting its vector property.

Note that we assumed that global deserts are covered by unvegetated dunes in this study. In addition, the naming directions of FP and RFP follows where the sand moves. Eventually, the ERA5-Land grid cells in deserts pile up sand measured by RFP under effective friction velocities.

Calculating the 72-year mean of sand flux

We estimated the spatial distributions of FP mean and RFP mean across global dunes. Considering the uncertainty of wind speed from the ERA5-Land hourly wind data[31], we extracted the spatial distributions of the standard deviations of the FP and RFP means during the study period (Fig. S1).

Area-weighted aggregated statistics

The means ± standard deviations of FP and RFP for global deserts were weighted by the grid cell area at a global scale, employing the CDO software[44].

Score criteria of wind and solar farms

According to the existing conceptual framework of sand flux[18-21], the FP and RFP means are divided into 18 and 8 classifications with the spacings of 10 m^2 yr^{-1} and 1.0 m^2 yr^{-1}, respectively. For wind and solar farms, the FP reflects wind energy, as well as the dust contamination and sand burial degrees on solar photovoltaic panel. Compared with high and large wind turbine[8], effective friction velocities drive dune movement, bring the sandblasting[27, 28], produce dusts that cover the solar panel surface, reducing the solar photovoltaic conversion efficiency[45], and cause severer sand burial to low solar photovoltaic panel. The RFP reflects the sand burial degree of solar photovoltaic panel and wind turbine in the resultant flux direction.

Thus, we proposed some simple criteria to score the suitability based on empirical judgment: First, high FP mean is favorable for wind farms. Second, high RFP mean would cause severer sand burial to solar generation infrastructure than wind generation infrastructure.

We assumed that FP mean is more important than RFP mean in scoring the suitability of wind and solar farms. On the basis of the aforementioned empirical judgment, we illustrated the detailed rules used for scoring the suitability of geometric intersections between classifications of FP mean and RFP mean:

Wind farms

For wind farms, we tabulated wind farm score according to the importance of empirical judgment about wind farms. The combination number of the FP and RFP mean classifications in sand flux was 144 (18×8).

The scoring scheme for wind farms included the following steps:

Step 1: Sort FP mean classification from low to high in the first column.

Step 2: In the second column, we sequentially nested RFP mean classification from high to low under individual classifications of FP mean (from low to high).

Step 3: Considering the empirical judgment about wind farms, we assigned the score from 1 to 144. However, only 80 combinations were observed at a global scale. The other 64 combinations did not exist, and their combinations, see Table S2. We removed these 64 combinations and reassigned the final wind farm score from 1 to 80 (Table S1).

Solar farms

For solar farms, we tabulated solar farm score by the importance of empirical judgment about solar farms (Table S3). The combination number of the FP and RFP mean classifications in sand flux was still 144 (18×8).

The scoring scheme for solar farms included the following steps:

Step 1: Sort FP mean classification in the first column from high to low.

Step 2: In the second column, we still sequentially nested RFP mean classification from high to low under individual classifications of FP mean (from low to high).

Step 3: Considering the empirical judgment about solar farms, we assigned the score from 1 to 144. However, only 80 combinations were observed at a global scale. The other 64 combinations did not exist, and their combinations, see Table S2. We removed these 64 combinations and reassigned the final solar farm score from 1 to 80 (Table S3).

Validation of the scoring scheme for solar farms in dune fields

The locations of solar farms used for the validation are from the global, open-access, harmonized spatial datasets based on the OpenStreetMap infrastructure data[33, 46]. We used the desert data to mask the point vector data titled by the global_solar_2020, and identified the actual locations of solar installations in deserts (Fig. S2), in order to validate the robustness of our scoring scheme for solar farms in deserts.

DATA AVAILABILITY

The dataset generated in this study are publicly available via the National Tibetan Plateau/Third Pole Environment Data Center (https://doi.org/10.11888/Terre.tpdc.272808).

CODE AVAILABILITY

Codes for calculating the yearly sand flux based on the ERA5-Land hourly wind data are available at https://github.com/liguoshuai-desert/wind-flux. Data analysis is finished by the CDO, Python, ArcGIS 10.6 and OriginPro Learning Edition software.

References

1 Arent, D. J., Wise, A. & Gelman, R. The status and prospects of renewable energy for combating global warming. *Energ. Econ.* **33**, 584-593 (2011).

2 Yang, Q. et al. Prospective contributions of biomass pyrolysis to China's 2050 carbon reduction and renewable energy goals. *Nat. Commun.* **12**, 1698 (2021).

3 United Naitons Environment Programme. *Emissions Gap Report 2021: The Heat Is On – A World of Climate Promises Not Yet Delivered*. Nairobi (2021).

4 Arias, P. A. et al. *Technical Summary*. in *Climate Change 2021: The Physical Science Basis. Contribution of Working Group I to the Sixth Assessment Report of the Intergovernmental Panel on Climate Change* [Masson-Delmotte V., P. Zhai, A. Pirani, S. L. Connors, C. Péan, S. Berger, N. Caud, Y. Chen, L. Goldfarb, M. I. Gomis, M. Huang, K. Leitzell, E. Lonnoy, J.B.R. Matthews, T. K. Maycock, T. Waterfield, O. Yelekçi, R. Yu and B. Zhou (eds.)]. Cambridge University Press, In Press (2021).

5 IPCC. *Summary for Policymakers*. In *Global Warming of 1.5°C. An IPCC Special Report on the impacts of global warming of 1.5°C above pre-industrial levels and related global greenhouse gas emission pathways, in the context of strengthening the global response to the threat of climate change, sustainable development, and efforts to eradicate poverty*. [Masson-Delmotte, V., P. Zhai, H.-O. Pörtner, D. Roberts, J. Skea, P.R. Shukla, A. Pirani, W. Moufouma-Okia, C. Péan, R. Pidcock, S. Connors, J.B.R. Matthews, Y. Chen, X. Zhou, M.I. Gomis, E. Lonnoy, T. Maycock, M. Tignor, and T. Waterfield (eds.)]. In Press (2018).

6 Fornasiero, P. & Graziani, M. *Renewable resources and renewable energy: a global challenge*. CRC press (2011).

7 Hao, F. & Shao, W. What really drives the deployment of renewable energy? A global assessment of 118 countries. *Energy Res. Soc. Sci.* **72**, 101880 (2021).

8 Veers, P. et al. Grand challenges in the science of wind energy. *Science* **366**, eaau2027 (2019).

9 Dowers, B. *Wind farms and solar PV panels in the landscape*. In *Reference Module in Earth Systems and Environmental Sciences*. Elsevier (2020).

10 Li Y. et al. Climate model shows large-scale wind and solar farms in the Sahara increase rain and vegetation. *Science* **361**, 1019-1022 (2018).

11 Lu, Z. et al. Impacts of large-scale Sahara solar farms on global climate and vegetation cover. *Geophys. Res. Lett.* **48**, e2020GL090789 (2021).

12 Moore, J. C., Jevrejeva, S. & Grinsted, A. Efficacy of geoengineering to limit 21st century sea-level rise. *Proc. Natl. Acad. Sci. USA* **107**, 15699-15703 (2010).

13 Matthews, H. D. & Caldeira, K. Transient climate–carbon simulations of planetary geoengineering. *Proc. Natl. Acad. Sci. USA* **104**, 9949-9954 (2007).

14. Al Garni, H. Z. & Awasthi, A. *Solar PV power plants site selection: a review*. In *Advances in Renewable Energies and Power Technologies*, [Yahyaoui, I. (ed.)]. Elsevier, 57-75 (2018).

15. Al-Dousari, A. et al. Solar and wind energy: Challenges and solutions in desert regions. *Energy* 176, 184-194 (2019).

16. Ehara, T., Komoto, K. & van der Vleuten, P. *Very large photovoltaic systems in deserts*. in *Reference Module in Earth Systems and Environmental Sciences. Elsevier* (2021).

17 Kocurek, G. *The aeolian rock record (Yes, Virginia, it exists, but it really is rather special to create one).* In *Aeolian Environments, Sediments and Landforms* [Andrew S. Goudie, Ian Livingstone, & Stephen Stokes (eds.)]. John Wiley and Sons Ltd, 239-259 (1999).

18 Gunn, A. et al., What sets aeolian dune height? *Nat. Commun.* **13**, 2401 (2022).

19 Gunn, A., East, A. & Jerolmack, D. J. 21st-century stagnation in unvegetated sand-sea activity. *Nat. Commun.* **13**, 3670 (2022).

20 Gunn, A. et al., Circadian rhythm of dune-field activity. *Geophys. Res. Lett.* **48**, e2020GL090924 (2021).

21 Chanteloube, C. et al., Source-to-sink aeolian fluxes from arid landscape dynamics in the Lut Desert. *Geophys. Res. Lett.* **49**, e2021GL097342 (2022).

22 Durán, O., Claudin, P. & Andreotti, B. On aeolian transport: Grain-scale interactions, dynamical mechanisms and scaling laws. *Aeolian. Res.* **3**, 243-270 (2011).

23 Martin, R. L. & Kok, J. F. Wind-invariant saltation heights imply linear scaling of aeolian saltation flux with shear stress. *Sci. Adv.* **3**, e1602569 (2017).

24 Jasper, F. K., Eric, J.-R.-P., Timothy, I. M. & Diana-Bou, K. The physics of wind-blown sand and dust. *Rep. Prog. Phys.* **75**, 106901 (2012).

25 Fryberger, S. G. Techniques for the evaluation of surface wind data in terms of eolian sand drift. United States Geological Survey, Open-File Report 78-405 (1978).

26 Fryberger, S. G. *Dune forms and wind regimes.* In *A study of global sand seas* [McKee, E. D. (ed)]. United States Geological Survey, 137-169 (1979).

27 Shao, Y. Physics and modelling of wind erosion (2nd ed.). (Springer Netherlands, 2008).

28 Kok, J. F. et al. An improved dust emission model – Part 1: Model description and comparison against measurements. Atmos. Chem. Phys. **14**, 13023-13041 (2014).

29 Yizhaq, H., Xu, Z. & Ashkenazy, Y. The effect of wind speed averaging time

on the calculation of sand drift potential: New scaling laws. *Earth and Planet. Sci. Lett.* **544**, 116373 (2020).
30 Hersbach, H. et al. The ERA5 global reanalysis. *Q. J. Roy. Meteor. Soc.* **146**, 1999-2049 (2020).
31 Muñoz-Sabater, J. et al. ERA5-Land: a state-of-the-art global reanalysis dataset for land applications. *Earth Syst. Sci. Data* **13**, 4349-4383 (2021).
32 Vermeesch, P. & Drake, N. Remotely sensed dune celerity and sand flux measurements of the world's fastest barchans (Bodélé, Chad). *Geophys. Res. Lett.* **35**, L24404 (2008).
33 Dunnett, S., Sorichetta, A., Taylor, G. & Eigenbrod, F. Harmonised global datasets of wind and solar farm locations and power. *Sci. Data* **7**, 130 (2020).
34 Kocurek, G. & Havholm, K. G. *Eolian sequence stratigraphy - a conceptual framework*. In *Siliciclastic sequence stratigraphy: recent developments and applications* [Weimer, P. and Posamentier, H. (eds.)], 393-409 (1993).
35 Lancaster, N. *Sand seas and dune fields*. In: Shroder, J. (Editor in Chief), Lancaster, N., Sherman, D.J., Baas, A.C.W. (Eds.), *Treatise on Geomorphology*. Academic Press, San Diego, CA, vol. 11, *Aeolian Geomorphology*, pp. 219–245 (2013).
36 Gadal, C. et al., Local wind regime induced by giant linear dunes: comparison of ERA5-Land Reanalysis with surface measurements. *Bound-Lay. Meteorol.* 185, 309-332 (2022).
37 Li, G. et al., More extreme precipitation in Chinese deserts from 1960 to 2018. *Earth Space Sci.* **6**, 1196-1204 (2019).
38 United Nations General Assembly. *Transforming our world: The 2030 agenda for sustainable development*. (December 2015).
39 Rogelj, J. et al. Zero emission targets as long-term global goals for climate protection. *Environ. Res. Lett.* **10**, 105007 (2015).
40 Wu, H. J., Lu, H. Y., Wang, J. J., Chen, Y. & Cui, M. C. A new estimate of global desert area and quantity of dust emission (in Chinese). *Chin. Sci. Bull.* **67**, 860-871 (2022).
41 Gunn, A. et al., Macroscopic flow disequilibrium over aeolian dune fields. *Geophys. Res. Lett.* **47**, e2020GL088773 (2020).
42 Greeley, R., Blumberg, D. G. & Williams, S. H. Field measurements of the flux and speed of wind-blown sand. *Sedimentology* **43**, 41-52 (1996).
43 Namikas, S. L. Field measurement and numerical modelling of aeolian mass flux distributions on a sandy beach. *Sedimentology* **50**, 303-326 (2003).
44 Mueller, R., Schulzweida, U., Kornbuleh, L. & Modali, K. Climate Data Operators (CDO) software, https://code.mpimet.mpg.de/projects/cdo (2013).
45 Bergin, M. H., Ghoroi, C., Dixit, D., Schauer, J. J. & Shindell, D. T. Large reductions in solar energy production due to dust and particulate air pollution. *Environ. Sci. Tech. Lett.* **4**, 339-344 (2017).
46 OpenStreetMap contributors. Elements. OpenStreetMap Wiki, https://wiki.openstreetmap.org/wiki/Elements (2019).

ACKNOWLEDGMENTS

We thank Xin Gao, Xiaolei Liang, Mengya Wang, Yani Li and Yingjun Pang for helping to collect dune samples. This research was supported by the National Natural Science Foundation of China (grant no. 41901377), and the Strategic Priority Research Program of Chinese Academy of Sciences under grant No. XDA20100104. F.C.L. was supported by the Swedish Research Council (Vetenskapsrådet, grant no. 2018-01272) and conducted the work with this article as a Pro Futura Scientia XIII Fellow funded by the Swedish Collegium for Advanced Study through Riksbankens Jubileumsfond.

AUTHOR CONTRIBUTIONS

G.L., L.T., B.Y. and X.L. designed research; G.L. and B.Y. performed research and analyzed data; G.L., L.T., T.C., Y.L., H.D., H.Z., Y.Z., C.H., R.J. and X.L. contributed analytic tools; G.L., L.T., B.Y., G.F., F.C.L., N.H., W.T. and X.L. wrote the paper.

COMPETING INTERESTS

The authors declare no competing interest.

ADDITIONAL INFORMATION

Supplementary Fig. S1–S2.
Supplementary Table S1–S4.

FIGURES

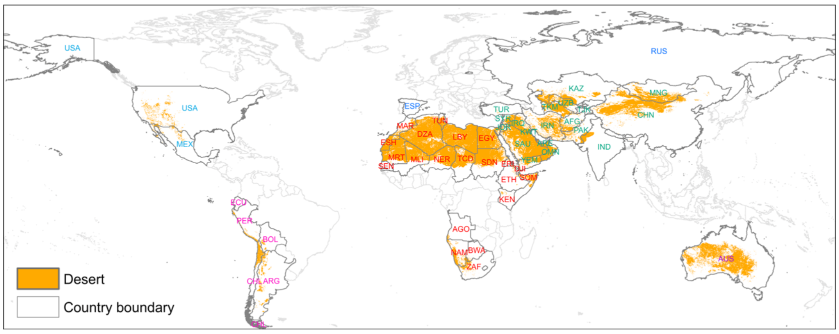

Fig. 1 Spatial distribution of global deserts.

Deserts are resampled to a resolution of 0.1°×0.1°, matching the spatial resolution of the ERA5-Land hourly wind data. Further, we use the 72-yr FP mean to constrain global deserts. The colored abbreviations are the three letter ISO 3166-1 alpha-3 GADM country codes. The countries in Asia are colored by the malachite green, the countries in Africa the mars red, the countries in South America the ginger pink, the countries in North America the moorea blue, the countries in Europe the cretan blue, and the countries in Australasia the anemone violet. The boundaries of the country with desert data are colored by 50% gray, and the rest are colored by 10% gray.

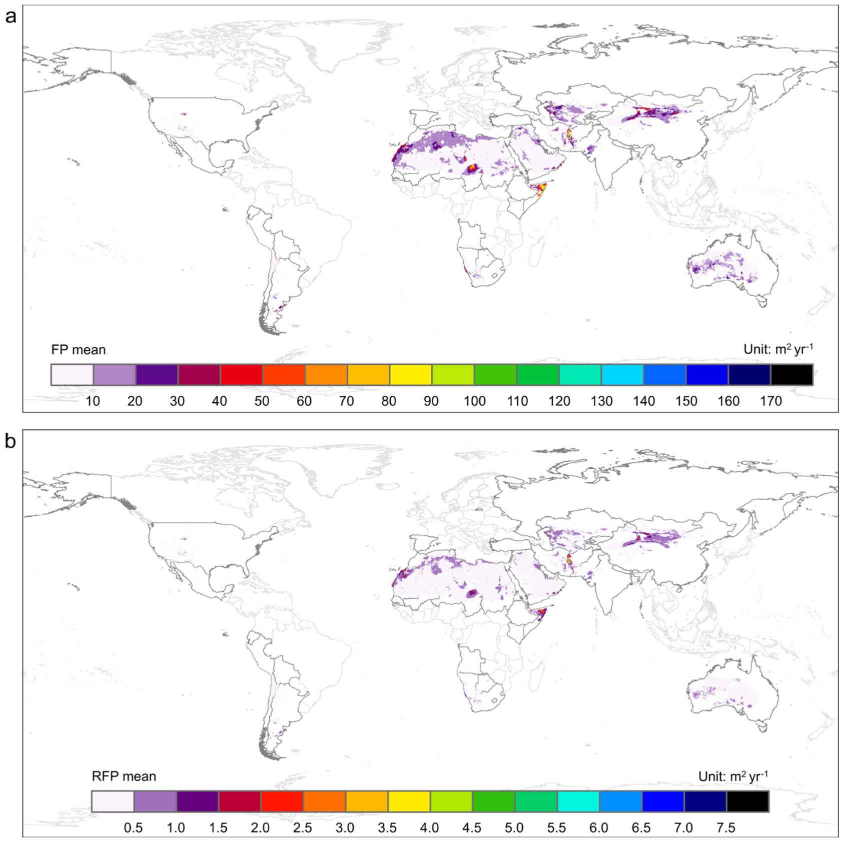

Fig. 2 The (a) FP and (b) RFP means of global deserts for the period 1950–2021.

The spacing of RFP mean is set to 0.5 m^2 yr^{-1}.

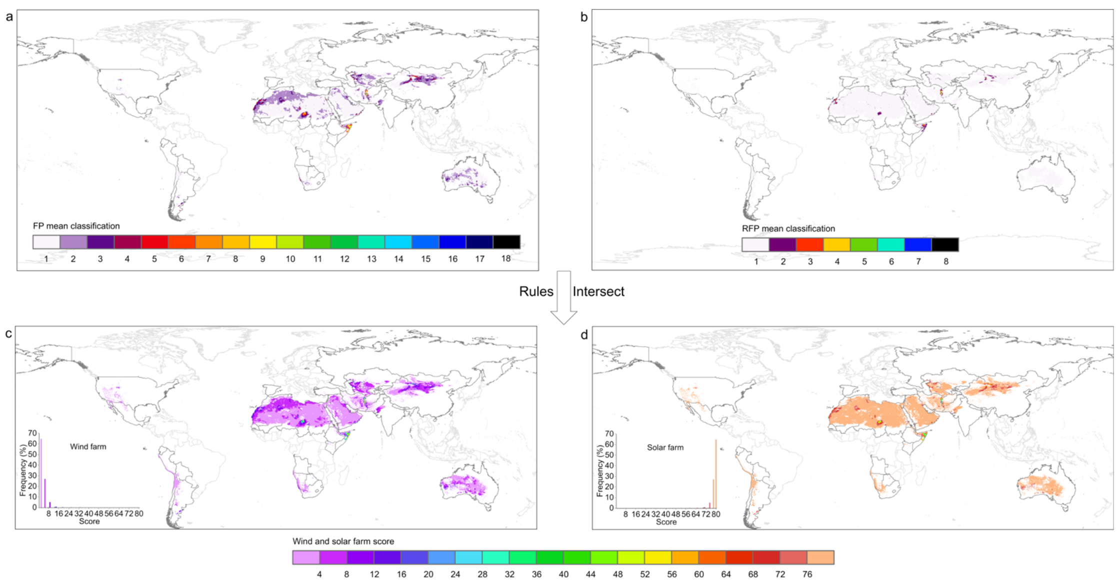

Fig. 3 The scoring scheme and result for wind and solar farms based on changes in sand flux.

First intersect the (**a**) FP and (**b**) RFP mean classifications, then remove non-observed combinations, and finally apply the established rules to assign the corresponding scores for wind farms (**c**) and solar farms (**d**). The bottom left insets show frequency distributions of wind and solar farm scores.

Supplementary Information

Site selection for desert wind and solar farms based on heterogeneous sand flux

Guoshuai Li, Lihai Tan, Bao Yang, Tao Che, Guangcai Feng, Fredrik Charpentier Ljungqvist, Yayong Luo, Heqiang Du, Hui Zhao, Ying Zhang, Chunlin Huang, Ning Huang, Wenjun Tang, Rui Jin, Xin Li

Corresponding email: Xin Li, xinli@itpcas.ac.cn

Supplementary Figures

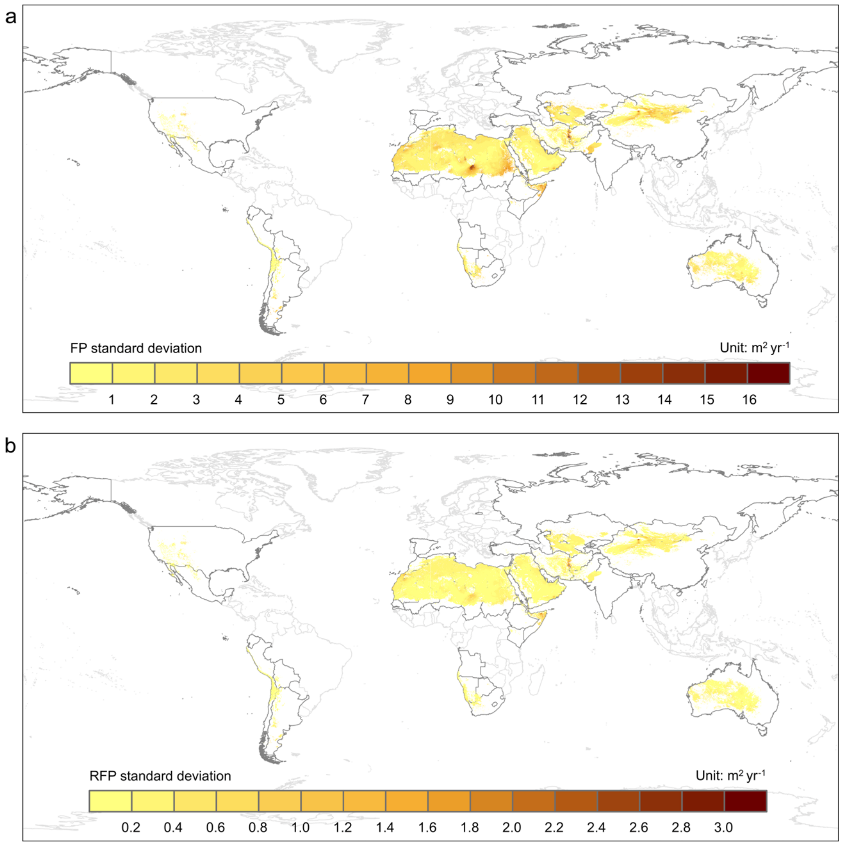

Fig. S1 Spatial distributions of the standard deviations of the (a) FP and (b) RFP for the period 1950–2021.

(a) and (b) adopt the interval size of 1 m^2 yr^{-1} and 0.2 m^2 yr^{-1}, respectively. The boundaries of the country with desert data are colored by 50% gray, and the rest are colored by 10% gray.

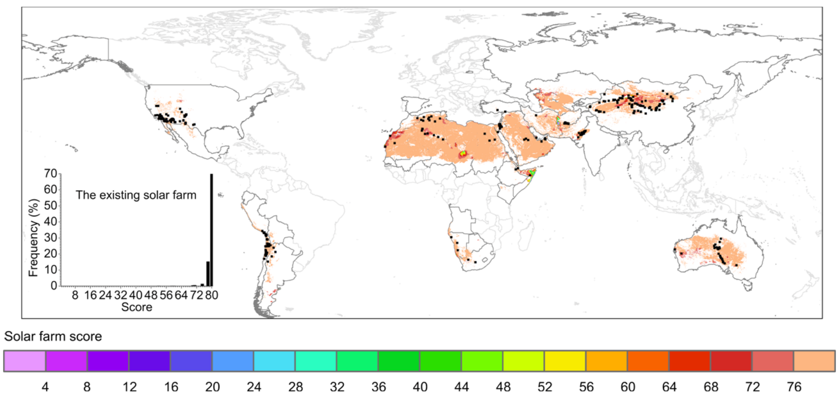

Fig. S2 Validation of solar farm score in deserts.

The black solid squares represent the locations of the 734 solar installations in deserts. The inset presents the scoring frequencies extracted by the existing solar farms in deserts, with score 52, accounting for 0.14% of the total; 59, 0.14%; 60, 0.14%; 70, 0.41%; 71, 0.54%; 75, 1.36%; 78, 15.26% and 80, 82.02%.

Supplementary Tables

Table S1. Wind farm score across global deserts.

FP mean is classified into 18 categories, and RFP mean is classified into 8 categories. High (low) score represents that wind farms have a strong (weak) suitability, but for building a real wind farm, we should choose the appropriate scores combined with other factors.

FP mean	RFP mean	Wind farm score
1	2	1
1	1	2
2	3	3
2	2	4
2	1	5
3	4	6
3	3	7
3	2	8
3	1	9
4	5	10
4	4	11
4	3	12
4	2	13
4	1	14
5	6	15
5	5	16
5	4	17
5	3	18
5	2	19
5	1	20
6	7	21
6	6	22
6	5	23
6	4	24
6	3	25
6	2	26
6	1	27
7	7	28
7	6	29
7	5	30
7	4	31
7	3	32
7	2	33
7	1	34
8	8	35
8	7	36

8	6	37
8	5	38
8	4	39
8	3	40
8	2	41
8	1	42
9	8	43
9	7	44
9	6	45
9	5	46
9	4	47
9	3	48
9	2	49
10	8	50
10	6	51
10	5	52
10	4	53
10	3	54
10	2	55
11	6	56
11	5	57
11	4	58
11	3	59
11	2	60
12	5	61
12	4	62
12	3	63
12	2	64
13	5	65
13	4	66
13	3	67
13	2	68
14	5	69
14	4	70
14	2	71
15	5	72
15	4	73
15	2	74
16	5	75
16	4	76
17	6	77
17	5	78
18	6	79
18	5	80

Table S2. The removed 64 combinations in Step 3 of wind farms and solar farms in METHODS.

FP mean	RFP mean
1	8
1	7
1	6
1	5
1	4
1	3
2	8
2	7
2	6
2	5
2	4
3	8
3	7
3	6
3	5
4	8
4	7
4	6
5	8
5	7
6	8
7	8
9	1
10	7
10	1
11	8
11	7
11	1
12	8
12	7
12	6
12	1
13	8
13	7
13	6
13	1
14	8
14	7
14	6
14	3
14	1

15	8
15	7
15	6
15	3
15	1
16	8
16	7
16	6
16	3
16	2
16	1
17	8
17	7
17	4
17	3
17	2
17	1
18	8
18	7
18	4
18	3
18	2
18	1

Table S3. Solar farm score across global dunes.

The same as Table S1, but for solar farms.

FP mean	RFP mean	Solar farm score
1	2	79
1	1	80
2	3	76
2	2	77
2	1	78
3	4	72
3	3	73
3	2	74
3	1	75
4	5	67
4	4	68
4	3	69
4	2	70
4	1	71
5	6	61
5	5	62
5	4	63
5	3	64
5	2	65
5	1	66
6	7	54
6	6	55
6	5	56
6	4	57
6	3	58
6	2	59
6	1	60
7	7	47
7	6	48
7	5	49
7	4	50
7	3	51
7	2	52
7	1	53
8	8	39
8	7	40
8	6	41
8	5	42
8	4	43
8	3	44

8	2	45
8	1	46
9	8	32
9	7	33
9	6	34
9	5	35
9	4	36
9	3	37
9	2	38
10	8	26
10	6	27
10	5	28
10	4	29
10	3	30
10	2	31
11	6	21
11	5	22
11	4	23
11	3	24
11	2	25
12	5	17
12	4	18
12	3	19
12	2	20
13	5	13
13	4	14
13	3	15
13	2	16
14	5	10
14	4	11
14	2	12
15	5	7
15	4	8
15	2	9
16	5	5
16	4	6
17	6	3
17	5	4
18	6	1
18	5	2

Table S4. The median grain diameters of dune samples in Chinese deserts.

In this study, Chinese desert with dune samples were the Taklamakan Desert (TakD), Gurban Tunggut Desert (GTD), Qaidam Desert (QaiD), Kumtag Desert (KumD), Badain Jaran Desert (BJD), Tengger Desert (TenD), Hobq Desert (HobD), Mu Us Sandy land (MUS), Hunshandake Sandy land (HunS), Hunlunbuir Sandy land (HulS) and Horqin Sandy land (HorS). The full names and corresponding abbreviations of Chinese deserts were referred to Li, G. et al.[35]. Particle size analysis of all sand samples were done with the Malvern laser granulometer (Malvern Mastersizer 3000). Dune samples above 10 cm depth in each desert in different sampling years were collected to analyze the median grain diameter (d_{50}).

No.	Name	Lon	Lat	d_{50} (mm)	Year	Provider
1	TakD	82.641	36.928	0.170	2017	Xin Gao
2	TakD	82.641	36.928	0.082	2017	Xin Gao
3	TakD	82.641	36.928	0.162	2017	Xin Gao
4	TakD	82.963	40.676	0.185	2017	Heqiang Du
5	TakD	84.197	41.307	0.149	2017	Heqiang Du
6	TakD	84.244	40.930	0.189	2017	Heqiang Du
7	TakD	84.297	40.734	0.154	2017	Heqiang Du
8	TakD	84.313	40.556	0.171	2017	Heqiang Du
9	TakD	84.328	40.384	0.150	2017	Heqiang Du
10	TakD	84.333	40.172	0.119	2017	Heqiang Du
11	TakD	84.264	39.966	0.126	2017	Heqiang Du
12	TakD	84.154	39.788	0.111	2017	Heqiang Du
13	TakD	83.987	39.571	0.132	2017	Heqiang Du
14	TakD	83.788	39.309	0.104	2017	Heqiang Du
15	TakD	83.622	39.027	0.133	2017	Heqiang Du
16	TakD	83.994	38.759	0.132	2017	Heqiang Du
17	TakD	84.303	38.602	0.116	2017	Heqiang Du
18	TakD	84.855	38.221	0.126	2017	Heqiang Du
19	TakD	88.421	39.660	0.101	2019	Lihai Tan
20	TakD	88.416	39.699	0.125	2019	Lihai Tan
21	TakD	88.384	39.811	0.119	2019	Lihai Tan
22	TakD	88.389	39.893	0.102	2019	Lihai Tan
23	TakD	88.361	39.958	0.111	2019	Lihai Tan
24	TakD	88.362	40.033	0.120	2019	Lihai Tan
25	TakD	88.244	40.228	0.162	2019	Lihai Tan
26	TakD	88.190	40.348	0.110	2019	Lihai Tan
27	TakD	87.986	40.462	0.115	2019	Lihai Tan
28	TakD	86.582	41.046	0.188	2019	Lihai Tan
29	TakD	86.582	41.046	0.202	2019	Lihai Tan
30	TakD	87.298	40.761	0.112	2019	Lihai Tan
31	TakD	87.298	40.761	0.143	2019	Lihai Tan
32	TakD	87.179	40.863	0.153	2019	Lihai Tan
33	TakD	79.969	37.283	0.176	2021	Lihai Tan
34	TakD	80.086	37.406	0.232	2021	Lihai Tan

35	TakD	80.267	37.508	0.246	2021	Lihai Tan
36	TakD	80.399	37.658	0.112	2021	Lihai Tan
37	TakD	80.518	37.794	0.108	2021	Lihai Tan
38	TakD	80.599	37.963	0.213	2021	Lihai Tan
39	TakD	80.636	38.128	0.221	2021	Lihai Tan
40	TakD	80.796	38.259	0.169	2021	Lihai Tan
41	TakD	80.933	38.397	0.180	2021	Lihai Tan
42	TakD	80.983	38.568	0.160	2021	Lihai Tan
43	TakD	80.974	38.784	0.170	2021	Lihai Tan
44	TakD	80.928	38.915	0.172	2021	Lihai Tan
45	TakD	80.950	39.101	0.169	2021	Lihai Tan
46	TakD	80.938	39.280	0.166	2021	Lihai Tan
47	TakD	80.971	39.439	0.168	2021	Lihai Tan
48	TakD	80.985	39.618	0.164	2021	Lihai Tan
49	TakD	80.964	39.799	0.179	2021	Lihai Tan
50	TakD	80.972	39.962	0.241	2021	Lihai Tan
51	TakD	81.009	40.147	0.237	2021	Lihai Tan
52	TakD	81.094	40.314	0.192	2021	Lihai Tan
53	TakD	83.626	39.035	0.131	2021	Lihai Tan
54	TakD	83.551	38.941	0.123	2021	Lihai Tan
55	TakD	83.455	38.804	0.138	2021	Lihai Tan
56	TakD	83.276	38.551	0.110	2021	Lihai Tan
57	TakD	83.173	38.306	0.133	2021	Lihai Tan
58	TakD	83.067	38.042	0.130	2021	Lihai Tan
59	TakD	82.986	37.721	0.130	2021	Lihai Tan
60	TakD	82.845	37.399	0.145	2021	Lihai Tan
61	TakD	87.011	38.692	0.198	2021	Lihai Tan
62	TakD	86.895	38.691	0.225	2021	Lihai Tan
63	TakD	86.647	38.714	0.181	2021	Lihai Tan
64	TakD	84.923	38.190	0.194	2021	Lihai Tan
65	TakD	84.859	38.217	0.186	2021	Lihai Tan
66	TakD	84.761	38.275	0.151	2021	Lihai Tan
67	TakD	84.589	38.378	0.138	2021	Lihai Tan
68	TakD	84.327	38.550	0.136	2021	Lihai Tan
69	TakD	84.043	38.719	0.142	2021	Lihai Tan
1	GTD	86.060	45.034	0.163	2017	Xin Gao
2	GTD	86.060	45.034	0.166	2017	Xin Gao
3	GTD	86.060	45.034	0.165	2017	Xin Gao
4	GTD	88.214	44.399	0.200	2021	Lihai Tan
5	GTD	88.299	44.503	0.272	2021	Lihai Tan
6	GTD	88.262	44.660	0.208	2021	Lihai Tan
7	GTD	88.312	44.842	0.311	2021	Lihai Tan
8	GTD	88.388	45.020	0.264	2021	Lihai Tan
9	GTD	88.279	45.133	0.280	2021	Lihai Tan

10	GTD	88.010	45.159	0.242	2021	Lihai Tan
11	GTD	87.764	45.228	0.227	2021	Lihai Tan
12	GTD	87.518	45.252	0.226	2021	Lihai Tan
13	GTD	87.232	45.291	0.285	2021	Lihai Tan
14	GTD	87.055	45.397	0.280	2021	Lihai Tan
15	GTD	86.764	45.452	0.284	2021	Lihai Tan
16	GTD	86.574	45.452	0.298	2021	Lihai Tan
17	GTD	88.634	46.377	0.373	2021	Lihai Tan
18	GTD	89.027	46.441	0.292	2021	Lihai Tan
19	GTD	88.758	44.946	0.296	2021	Lihai Tan
20	GTD	88.614	44.946	0.330	2021	Lihai Tan
21	GTD	88.480	44.949	0.242	2021	Lihai Tan
22	GTD	88.388	44.967	0.411	2021	Lihai Tan
23	GTD	89.127	44.604	0.191	2021	Lihai Tan
24	GTD	89.146	44.538	0.207	2021	Lihai Tan
25	GTD	89.164	44.377	0.191	2021	Lihai Tan
26	GTD	89.165	44.294	0.208	2021	Lihai Tan
1	QaiD	91.792	37.974	0.268	2017	Lihai Tan
2	QaiD	91.792	37.975	0.276	2017	Lihai Tan
3	QaiD	91.792	37.974	0.225	2017	Lihai Tan
4	QaiD	97.956	36.408	0.304	2020	Lihai Tan
5	QaiD	97.946	36.410	0.235	2020	Lihai Tan
6	QaiD	97.940	36.415	0.170	2020	Lihai Tan
7	QaiD	97.928	36.419	0.286	2020	Lihai Tan
8	QaiD	97.914	36.413	0.228	2020	Lihai Tan
9	QaiD	97.901	36.410	0.241	2020	Lihai Tan
10	QaiD	97.890	36.407	0.287	2020	Lihai Tan
11	QaiD	97.867	36.408	0.245	2020	Lihai Tan
12	QaiD	97.874	36.418	0.191	2020	Lihai Tan
13	QaiD	97.882	36.425	0.162	2020	Lihai Tan
14	QaiD	97.895	36.433	0.169	2020	Lihai Tan
15	QaiD	97.912	36.437	0.244	2020	Lihai Tan
16	QaiD	97.924	36.439	0.148	2020	Lihai Tan
17	QaiD	97.941	36.442	0.132	2020	Lihai Tan
18	QaiD	97.956	36.440	0.173	2020	Lihai Tan
19	QaiD	98.110	36.421	0.217	2020	Lihai Tan
20	QaiD	98.121	36.422	0.196	2020	Lihai Tan
21	QaiD	98.131	36.424	0.209	2020	Lihai Tan
22	QaiD	94.203	37.924	0.235	2020	Lihai Tan
23	QaiD	94.208	37.936	0.238	2020	Lihai Tan
24	QaiD	94.200	37.907	0.174	2020	Lihai Tan
25	QaiD	94.197	37.883	0.196	2020	Lihai Tan
26	QaiD	94.191	37.856	0.174	2020	Lihai Tan
27	QaiD	94.169	37.444	0.238	2020	Lihai Tan

28	QaiD	94.132	37.406	0.176	2020	Lihai Tan
29	QaiD	93.851	37.610	0.155	2020	Lihai Tan
30	QaiD	92.714	38.483	0.275	2020	Lihai Tan
31	QaiD	93.274	38.663	0.227	2020	Lihai Tan
32	QaiD	91.196	37.877	0.292	2020	Lihai Tan
33	QaiD	91.190	37.870	0.253	2020	Lihai Tan
34	QaiD	92.889	37.007	0.191	2020	Lihai Tan
1	KumD	92.549	40.245	0.257	2018	Xiaolei Liang
2	KumD	92.895	40.432	0.244	2018	Xiaolei Liang
3	KumD	92.841	40.404	0.309	2018	Xiaolei Liang
4	KumD	92.487	40.209	0.177	2018	Xiaolei Liang
5	KumD	92.546	40.289	0.259	2018	Xiaolei Liang
6	KumD	93.078	40.466	0.382	2018	Xiaolei Liang
7	KumD	93.025	40.432	0.305	2018	Xiaolei Liang
8	KumD	92.559	40.411	0.393	2018	Xiaolei Liang
9	KumD	92.276	40.333	0.219	2018	Xiaolei Liang
10	KumD	92.965	40.411	0.352	2018	Xiaolei Liang
11	KumD	92.603	40.132	0.314	2018	Yingjun Pang
12	KumD	94.121	39.927	0.153	2020	Lihai Tan
13	KumD	94.128	39.941	0.162	2020	Lihai Tan
14	KumD	94.006	39.934	0.171	2020	Lihai Tan
15	KumD	94.008	39.965	0.160	2020	Lihai Tan
16	KumD	93.993	40.099	0.158	2020	Lihai Tan
17	KumD	93.982	40.118	0.141	2020	Lihai Tan
18	KumD	94.353	39.760	0.171	2020	Lihai Tan
19	KumD	94.352	39.751	0.125	2020	Lihai Tan
20	KumD	94.350	39.741	0.118	2020	Lihai Tan
21	KumD	94.355	39.726	0.122	2020	Lihai Tan
22	KumD	94.347	39.702	0.121	2020	Lihai Tan
1	BJD	102.488	39.870	0.256	2014	Hui Zhao
2	BJD	102.477	39.876	0.168	2017	Hui Zhao
3	BJD	102.502	39.859	0.274	2017	Hui Zhao
4	BJD	102.620	39.833	0.193	2018	Hui Zhao
5	BJD	101.535	40.087	0.196	2018	Hui Zhao
6	BJD	102.075	40.058	0.167	2018	Hui Zhao
7	BJD	101.791	39.989	0.183	2018	Hui Zhao
8	BJD	102.274	39.915	0.216	2018	Hui Zhao
9	BJD	102.502	39.860	0.288	2018	Hui Zhao
10	BJD	101.117	40.126	0.217	2018	Hui Zhao
11	BJD	102.236	39.973	0.255	2018	Hui Zhao
12	BJD	102.273	39.915	0.215	2018	Hui Zhao
13	BJD	101.397	40.168	0.262	2018	Hui Zhao
14	BJD	102.366	39.554	0.261	2019	Mengya Wang
15	BJD	102.365	39.551	0.265	2019	Mengya Wang

16	BJD	102.667	39.337	0.194	2019	Mengya Wang
17	BJD	102.667	39.339	0.168	2019	Mengya Wang
18	BJD	102.666	39.336	0.183	2019	Mengya Wang
1	TenD	105.080	37.686	0.177	2018	Yani Li
2	TenD	105.074	37.687	0.187	2018	Yani Li
3	TenD	105.065	37.686	0.248	2018	Yani Li
4	TenD	105.063	37.686	0.239	2018	Yani Li
1	HobD	107.277	40.446	0.250	2021	Guoshuai Li
2	HobD	107.433	40.581	0.243	2021	Guoshuai Li
3	HobD	107.580	40.575	0.226	2021	Guoshuai Li
4	HobD	107.626	40.435	0.247	2021	Guoshuai Li
5	HobD	107.682	40.174	0.167	2021	Guoshuai Li
6	HobD	107.612	40.745	0.215	2021	Guoshuai Li
7	HobD	107.921	40.769	0.191	2021	Guoshuai Li
8	HobD	108.085	40.796	0.242	2021	Guoshuai Li
9	HobD	108.224	40.803	0.228	2021	Guoshuai Li
10	HobD	108.356	40.774	0.210	2021	Guoshuai Li
11	HobD	108.391	40.717	0.239	2021	Guoshuai Li
12	HobD	108.448	40.631	0.216	2021	Guoshuai Li
13	HobD	108.352	40.657	0.214	2021	Guoshuai Li
14	HobD	108.267	40.679	0.213	2021	Guoshuai Li
15	HobD	108.321	40.692	0.238	2021	Guoshuai Li
16	HobD	108.633	40.459	0.223	2021	Guoshuai Li
17	HobD	108.559	40.313	0.233	2021	Guoshuai Li
18	HobD	108.502	40.259	0.212	2021	Guoshuai Li
19	HobD	108.660	39.916	0.266	2021	Guoshuai Li
20	HobD	108.693	39.948	0.220	2021	Guoshuai Li
21	HobD	108.963	39.867	0.245	2021	Guoshuai Li
22	HobD	108.834	39.995	0.211	2021	Guoshuai Li
23	HobD	108.917	40.414	0.190	2021	Guoshuai Li
24	HobD	109.010	40.360	0.178	2021	Guoshuai Li
25	HobD	109.042	40.263	0.219	2021	Guoshuai Li
26	HobD	109.383	40.338	0.183	2021	Guoshuai Li
27	HobD	109.415	40.308	0.191	2021	Guoshuai Li
28	HobD	109.809	40.270	0.187	2021	Guoshuai Li
29	HobD	109.799	40.234	0.184	2021	Guoshuai Li
30	HobD	110.503	40.154	0.184	2021	Guoshuai Li
31	HobD	111.039	40.145	0.197	2021	Guoshuai Li
32	HobD	110.981	40.133	0.220	2021	Guoshuai Li
1	MUS	107.524	37.949	0.232	2020	Guoshuai Li
2	MUS	107.524	37.949	0.238	2020	Guoshuai Li
3	MUS	107.638	37.919	0.208	2020	Guoshuai Li
4	MUS	107.638	37.919	0.190	2020	Guoshuai Li
5	MUS	107.723	37.901	0.190	2020	Guoshuai Li

6	MUS	107.776	37.914	0.201	2020	Guoshuai Li
7	MUS	107.909	37.902	0.211	2020	Guoshuai Li
8	MUS	108.572	37.739	0.168	2020	Guoshuai Li
9	MUS	108.704	37.801	0.198	2020	Guoshuai Li
10	MUS	108.533	38.065	0.206	2020	Guoshuai Li
11	MUS	108.660	38.171	0.234	2020	Guoshuai Li
12	MUS	108.778	38.491	0.233	2020	Guoshuai Li
13	MUS	109.484	38.488	0.209	2020	Guoshuai Li
14	MUS	109.650	38.557	0.249	2020	Guoshuai Li
15	MUS	109.663	38.700	0.318	2020	Guoshuai Li
16	MUS	109.649	38.711	0.273	2020	Guoshuai Li
17	MUS	109.710	38.820	0.274	2020	Guoshuai Li
18	MUS	109.722	38.892	0.282	2020	Guoshuai Li
19	MUS	109.793	38.925	0.383	2020	Guoshuai Li
20	MUS	109.701	38.926	0.257	2020	Guoshuai Li
21	MUS	109.611	38.909	0.299	2020	Guoshuai Li
22	MUS	109.447	38.909	0.260	2020	Guoshuai Li
23	MUS	109.400	38.977	0.323	2020	Guoshuai Li
24	MUS	109.295	38.967	0.246	2020	Guoshuai Li
25	MUS	109.182	38.918	0.294	2020	Guoshuai Li
26	MUS	109.107	39.013	0.272	2020	Guoshuai Li
27	MUS	109.042	39.069	0.273	2020	Guoshuai Li
28	MUS	109.042	39.126	0.290	2020	Guoshuai Li
29	MUS	109.053	39.192	0.318	2020	Guoshuai Li
30	MUS	108.973	39.307	0.358	2020	Guoshuai Li
31	MUS	108.969	39.231	0.312	2020	Guoshuai Li
32	MUS	108.899	39.218	0.231	2020	Guoshuai Li
33	MUS	108.890	39.183	0.298	2020	Guoshuai Li
34	MUS	108.743	39.211	0.336	2020	Guoshuai Li
35	MUS	108.663	39.211	0.322	2020	Guoshuai Li
36	MUS	108.645	39.162	0.322	2020	Guoshuai Li
37	MUS	108.634	39.122	0.327	2020	Guoshuai Li
38	MUS	108.584	39.095	0.334	2020	Guoshuai Li
39	MUS	108.547	39.059	0.291	2020	Guoshuai Li
40	MUS	108.551	38.975	0.281	2020	Guoshuai Li
41	MUS	108.576	38.896	0.276	2020	Guoshuai Li
42	MUS	108.567	38.839	0.244	2020	Guoshuai Li
43	MUS	108.551	38.777	0.280	2020	Guoshuai Li
44	MUS	108.438	38.837	0.327	2020	Guoshuai Li
45	MUS	108.257	38.884	0.328	2020	Guoshuai Li
46	MUS	108.279	38.762	0.326	2020	Guoshuai Li
47	MUS	108.374	38.637	0.248	2020	Guoshuai Li
48	MUS	108.304	38.589	0.294	2020	Guoshuai Li
49	MUS	108.347	38.607	0.269	2020	Guoshuai Li

50	MUS	108.195	38.530	0.278	2020	Guoshuai Li
51	MUS	108.141	38.479	0.260	2020	Guoshuai Li
52	MUS	108.090	38.396	0.205	2020	Guoshuai Li
53	MUS	107.998	38.354	0.196	2020	Guoshuai Li
54	MUS	107.782	38.362	0.217	2020	Guoshuai Li
55	MUS	107.737	38.379	0.273	2020	Guoshuai Li
56	MUS	107.654	38.407	0.286	2020	Guoshuai Li
57	MUS	107.591	38.385	0.232	2020	Guoshuai Li
58	MUS	107.529	38.313	0.194	2020	Guoshuai Li
59	MUS	107.467	38.150	0.248	2020	Guoshuai Li
1	HunS	115.814	42.618	0.178	2019	Yayong Luo
2	HunS	116.074	42.579	0.163	2019	Yayong Luo
3	HunS	115.370	42.794	0.217	2019	Yayong Luo
4	HunS	115.631	42.743	0.233	2019	Yayong Luo
5	HunS	115.899	43.219	0.115	2019	Yayong Luo
6	HunS	116.067	42.954	0.199	2019	Yayong Luo
7	HunS	116.090	43.224	0.196	2019	Yayong Luo
8	HunS	115.984	42.853	0.240	2019	Yayong Luo
9	HunS	117.070	43.038	0.177	2019	Yayong Luo
10	HunS	116.646	42.672	0.185	2019	Yayong Luo
11	HunS	115.136	42.760	0.180	2019	Yayong Luo
12	HunS	115.264	42.856	0.240	2019	Yayong Luo
13	HunS	114.919	42.967	0.201	2019	Yayong Luo
14	HunS	115.013	42.919	0.184	2019	Yayong Luo
15	HunS	114.400	42.994	0.213	2019	Yayong Luo
16	HunS	117.030	42.998	0.259	2019	Yayong Luo
17	HunS	117.056	42.995	0.239	2019	Yayong Luo
18	HunS	114.742	43.066	0.340	2019	Yayong Luo
19	HunS	112.433	43.100	0.267	2021	Guoshuai Li
20	HunS	112.414	43.128	0.256	2021	Guoshuai Li
21	HunS	112.195	43.151	0.294	2021	Guoshuai Li
22	HunS	112.198	43.100	0.236	2021	Guoshuai Li
23	HunS	112.489	43.122	0.289	2021	Guoshuai Li
24	HunS	112.859	43.077	0.257	2021	Guoshuai Li
25	HunS	112.932	43.153	0.345	2021	Guoshuai Li
26	HunS	112.988	43.217	0.286	2021	Guoshuai Li
27	HunS	113.487	43.213	0.311	2021	Guoshuai Li
28	HunS	113.531	43.196	0.308	2021	Guoshuai Li
29	HunS	113.449	43.179	0.270	2021	Guoshuai Li
30	HunS	113.430	43.143	0.272	2021	Guoshuai Li
31	HunS	113.366	43.157	0.297	2021	Guoshuai Li
32	HunS	113.343	43.139	0.236	2021	Guoshuai Li
33	HunS	113.328	43.097	0.275	2021	Guoshuai Li
34	HunS	113.681	43.199	0.280	2021	Guoshuai Li

35	HunS	113.710	43.175	0.267	2021	Guoshuai Li
36	HunS	113.736	43.057	0.267	2021	Guoshuai Li
37	HunS	113.812	43.112	0.253	2021	Guoshuai Li
38	HunS	113.586	43.227	0.259	2021	Guoshuai Li
39	HunS	114.463	43.254	0.221	2021	Guoshuai Li
40	HunS	114.484	43.128	0.255	2021	Guoshuai Li
41	HunS	114.505	43.054	0.290	2021	Guoshuai Li
42	HunS	114.543	43.002	0.266	2021	Guoshuai Li
43	HunS	114.503	42.943	0.237	2021	Guoshuai Li
44	HunS	114.561	42.893	0.270	2021	Guoshuai Li
45	HunS	116.129	43.174	0.231	2021	Guoshuai Li
46	HunS	116.020	43.053	0.261	2021	Guoshuai Li
47	HunS	115.898	42.870	0.196	2021	Guoshuai Li
48	HunS	115.892	42.776	0.236	2021	Guoshuai Li
49	HunS	115.944	42.690	0.221	2021	Guoshuai Li
50	HunS	115.838	42.620	0.257	2021	Guoshuai Li
51	HunS	115.984	42.600	0.268	2021	Guoshuai Li
52	HunS	115.988	42.670	0.241	2021	Guoshuai Li
53	HunS	116.183	42.762	0.226	2021	Guoshuai Li
54	HunS	116.425	42.860	0.222	2021	Guoshuai Li
55	HunS	116.834	43.005	0.318	2021	Guoshuai Li
1	HulS	119.306	49.097	0.230	2021	Guoshuai Li
2	HulS	119.301	49.083	0.273	2021	Guoshuai Li
3	HulS	119.235	49.072	0.267	2021	Guoshuai Li
4	HulS	119.236	49.086	0.253	2021	Guoshuai Li
5	HulS	119.215	49.107	0.201	2021	Guoshuai Li
6	HulS	119.211	49.121	0.223	2021	Guoshuai Li
7	HulS	119.129	49.139	0.241	2021	Guoshuai Li
8	HulS	118.857	49.143	0.235	2021	Guoshuai Li
9	HulS	118.811	49.127	0.223	2021	Guoshuai Li
10	HulS	118.805	49.102	0.305	2021	Guoshuai Li
11	HulS	118.645	49.130	0.276	2021	Guoshuai Li
12	HulS	118.550	49.141	0.253	2021	Guoshuai Li
13	HulS	118.449	49.237	0.302	2021	Guoshuai Li
14	HulS	118.402	49.410	0.294	2021	Guoshuai Li
15	HulS	118.224	48.264	0.383	2021	Guoshuai Li
16	HulS	118.342	48.244	0.337	2021	Guoshuai Li
17	HulS	118.337	48.248	0.275	2021	Guoshuai Li
18	HulS	118.466	48.274	0.212	2021	Guoshuai Li
19	HulS	118.628	48.563	0.297	2021	Guoshuai Li
20	HulS	118.621	48.563	0.242	2021	Guoshuai Li
21	HulS	118.532	48.592	0.303	2021	Guoshuai Li
22	HulS	118.498	48.608	0.307	2021	Guoshuai Li
23	HulS	118.552	48.403	0.255	2021	Guoshuai Li

24	HulS	118.512	48.427	0.237	2021	Guoshuai Li
25	HulS	118.344	48.340	0.276	2021	Guoshuai Li
26	HulS	118.318	48.269	0.234	2021	Guoshuai Li
27	HulS	118.310	48.280	0.269	2021	Guoshuai Li
28	HulS	118.317	48.192	0.253	2021	Guoshuai Li
29	HulS	118.438	48.201	0.368	2021	Guoshuai Li
30	HulS	118.422	48.197	0.466	2021	Guoshuai Li
31	HulS	118.463	48.154	0.276	2021	Guoshuai Li
32	HulS	118.626	48.190	0.283	2021	Guoshuai Li
33	HulS	118.760	48.196	0.380	2021	Guoshuai Li
34	HulS	118.916	48.238	0.269	2021	Guoshuai Li
35	HulS	118.954	48.251	0.271	2021	Guoshuai Li
36	HulS	118.808	48.255	0.299	2021	Guoshuai Li
37	HulS	118.304	48.166	0.328	2021	Guoshuai Li
1	HorS	119.232	43.111	0.191	2018	Yayong Luo
2	HorS	119.210	43.029	0.158	2018	Yayong Luo
3	HorS	119.233	43.159	0.175	2018	Yayong Luo
4	HorS	119.289	43.063	0.182	2018	Yayong Luo
5	HorS	121.911	42.813	0.264	2018	Yayong Luo
6	HorS	121.789	42.870	0.220	2018	Yayong Luo
7	HorS	120.804	43.328	0.256	2018	Yayong Luo
8	HorS	120.746	43.187	0.242	2018	Yayong Luo
9	HorS	120.719	43.089	0.205	2018	Yayong Luo
10	HorS	120.677	43.282	0.199	2018	Yayong Luo
11	HorS	120.604	43.187	0.177	2018	Yayong Luo
12	HorS	120.477	43.140	0.272	2018	Yayong Luo
13	HorS	120.461	43.205	0.230	2018	Yayong Luo
14	HorS	120.405	43.034	0.326	2018	Yayong Luo
15	HorS	120.368	43.203	0.218	2018	Yayong Luo
16	HorS	120.312	43.064	0.240	2018	Yayong Luo
17	HorS	120.274	42.965	0.219	2018	Yayong Luo
18	HorS	119.867	42.886	0.275	2018	Yayong Luo
19	HorS	119.689	43.206	0.178	2018	Yayong Luo
20	HorS	119.497	42.860	0.126	2019	Yayong Luo
21	HorS	118.972	43.114	0.145	2019	Yayong Luo
22	HorS	118.180	43.539	0.328	2021	Guoshuai Li
23	HorS	118.210	43.498	0.337	2021	Guoshuai Li
24	HorS	118.403	43.556	0.274	2021	Guoshuai Li
25	HorS	119.979	44.462	0.219	2021	Guoshuai Li
26	HorS	120.089	44.383	0.296	2021	Guoshuai Li
27	HorS	120.127	44.332	0.260	2021	Guoshuai Li
28	HorS	120.121	44.324	0.262	2021	Guoshuai Li
29	HorS	120.157	44.346	0.414	2021	Guoshuai Li
30	HorS	120.261	44.268	0.359	2021	Guoshuai Li

31	HorS	120.365	44.209	0.279	2021	Guoshuai Li
32	HorS	120.328	44.165	0.255	2021	Guoshuai Li
33	HorS	120.450	44.032	0.275	2021	Guoshuai Li
34	HorS	120.459	44.028	0.236	2021	Guoshuai Li
35	HorS	120.564	43.938	0.221	2021	Guoshuai Li
36	HorS	120.590	43.925	0.359	2021	Guoshuai Li
37	HorS	120.595	43.952	0.305	2021	Guoshuai Li
38	HorS	120.614	44.041	0.259	2021	Guoshuai Li
39	HorS	120.636	44.070	0.271	2021	Guoshuai Li
40	HorS	120.603	43.765	0.209	2021	Guoshuai Li
41	HorS	120.619	43.757	0.220	2021	Guoshuai Li
42	HorS	120.921	43.326	0.279	2021	Guoshuai Li
43	HorS	120.873	43.311	0.315	2021	Guoshuai Li
44	HorS	120.846	43.278	0.277	2021	Guoshuai Li
45	HorS	120.845	43.255	0.277	2021	Guoshuai Li
46	HorS	120.788	43.217	0.257	2021	Guoshuai Li
47	HorS	120.720	43.235	0.285	2021	Guoshuai Li
48	HorS	120.673	43.282	0.275	2021	Guoshuai Li
49	HorS	120.693	43.170	0.274	2021	Guoshuai Li
50	HorS	120.607	43.184	0.215	2021	Guoshuai Li
51	HorS	120.594	43.117	0.291	2021	Guoshuai Li
52	HorS	120.535	43.025	0.242	2021	Guoshuai Li
53	HorS	120.405	43.029	0.236	2021	Guoshuai Li
54	HorS	120.461	42.921	0.254	2021	Guoshuai Li
55	HorS	120.857	42.776	0.272	2021	Guoshuai Li
56	HorS	120.599	42.780	0.226	2021	Guoshuai Li
57	HorS	120.306	43.067	0.228	2021	Guoshuai Li
58	HorS	120.238	43.140	0.338	2021	Guoshuai Li
59	HorS	119.976	43.197	0.267	2021	Guoshuai Li
60	HorS	119.992	43.119	0.266	2021	Guoshuai Li
61	HorS	120.048	43.062	0.243	2021	Guoshuai Li
62	HorS	119.679	42.905	0.326	2021	Guoshuai Li
63	HorS	119.607	43.103	0.231	2021	Guoshuai Li
64	HorS	119.567	43.189	0.309	2021	Guoshuai Li
65	HorS	119.406	43.201	0.245	2021	Guoshuai Li
66	HorS	119.319	43.095	0.254	2021	Guoshuai Li
67	HorS	119.237	43.021	0.266	2021	Guoshuai Li
68	HorS	119.178	43.013	0.274	2021	Guoshuai Li
69	HorS	120.736	42.977	0.246	2021	Yayong Luo
70	HorS	120.714	42.941	0.198	2021	Yayong Luo